



Spallation-induced roughness promoting high spatial frequency nanostructure formation on Cr

A. Abou-Saleh¹ · E. T. Karim^{2,3} · C. Maurice⁴ · S. Reynaud¹ · F. Pigeon¹ · F. Garrelie¹ · L. V. Zhigilei² · J. P. Colombier¹

Received: 31 October 2017 / Accepted: 2 March 2018
© Springer-Verlag GmbH Germany, part of Springer Nature 2018

Abstract

Interaction of ultrafast laser pulses with metal surfaces in the spallation regime can result in the formation of anisotropic nanoscale surface morphology commonly referred to as laser-induced periodic surface structures (LIPSS) or ripples. The surface structures generated by a single pulse irradiation of monocrystalline Cr samples are investigated experimentally and computationally for laser fluences that produce high spatial frequency nanostructures in the multi-pulse irradiation regime. Electron microscopy reveals distinct response of samples with different crystallographic surface orientations, with (100) surfaces exhibiting the formation of more refined nanostructure by a single pulse irradiation and a more pronounced LIPSS after two laser pulses as compared to (110) surfaces. A large-scale molecular dynamics simulation of laser interaction with a (100) Cr target provides detailed information on processes responsible for spallation of a liquid layer, redistribution of molten material, and rapid resolidification of the target. The nanoscale roughness of the resolidified surface predicted in the simulation features elongated frozen nanospikes, nanorims and nanocavities with dimensions and surface density similar to those in the surface morphology observed for (100) Cr target with atomic force microscopy. The results of the simulation suggest that the types, sizes and dimensions of the nanoscale surface features are defined by the competition between the evolution of transient liquid structures generated in the spallation process and the rapid resolidification of the surface region of the target. The spallation-induced roughness is likely to play a key role in triggering the generation of high-frequency LIPSS upon irradiation by multiple laser pulses.

1 Introduction

Ultrashort (femtosecond to picosecond) laser pulses are in the core of many innovative technologies, which impact a broad range of applications in the fields of photonics and

biomedicine [1–4]. The application of ultrashort laser pulses reduces the heat affected zone in material processing and machining [5], thus enabling material modification with high accuracy and spatial resolution [6]. One of the remarkable features of ultrashort laser interactions with surfaces is the ability to produce laser-induced periodic surface structures (LIPSS), which has been demonstrated for different materials [7, 8] and is finding an increasing utilization in practical applications [9–12]. The LIPSS-covered surfaces may exhibit structural color, which is used for permanent coloring of large surface regions or selective color marking [13–17]. The LIPSS are also of high importance for medical applications, where the reduction of cell adhesion and enhancement of osseointegration of nano/micro-structured surfaces facilitate the integration and increase the life span of the implants [18–20]. Other examples include tribological applications [21–25], as well as analytical techniques relying on surface enhanced Raman scattering (SERS), where spectroscopic signal can be greatly improved via plasmonic excitation near the nanoscale surface features [26–28].

A. Abou-Saleh and E. T. Karim contributed equally to this work.

✉ J. P. Colombier
jean.philippe.colombier@univ-st-etienne.fr

¹ Univ Lyon, UJM-Saint-Etienne, CNRS, Institut d'Optique Graduate School, Laboratoire Hubert-Curien UMR5516, 42023 Saint-Étienne, France

² Department of Materials Science and Engineering, University of Virginia, 395 McCormick Road, Charlottesville, VA 22904-4745, USA

³ Department of Materials Science and Engineering, University of Maryland, 4418 Stadium Dr., College Park, MD 20742-2115, USA

⁴ Laboratoire Georges Friedel, CNRS, UMR 5307, Ecole Nationale Supérieure des Mines de Saint-Etienne, 42023 Saint-Étienne, France

The formation of LIPSS is typically occurring in multi-pulse irradiation regime, where the first pulse with a fluence below the ablation threshold perturbs the surface morphology, while irradiation by additional pulses at the same fluence results in the formation of LIPSS or, more precisely, low spatial frequency LIPSS (LSFLs) with periodicity close to the laser wavelength. The formation of LSFLs is typically attributed to the interference between the incident laser light and a surface scattered electromagnetic wave [29], which causes inhomogeneous energy deposition at the illuminated surface [30, 31] and subsequent material redistribution. Due to the high intensity of ultra-short laser pulses, this mechanism of the LIPSS formation can be activated in almost all types of materials, including metals, semiconductors, dielectrics, and polymers [32–34]. Moreover, in addition to LSFLs oriented perpendicular to the laser beam polarization, high-spatial frequency LIPSS (HSFLs) with periods significantly smaller than the laser wavelength and an orientation that can be either parallel or perpendicular to the polarization can be generated [35, 36].

The mechanisms of the LIPSS formation are still actively debated in literature [7, 8, 37–41], and a detailed chemical and microstructural analysis of samples exposed to the laser processing may provide important clues to the key processes responsible for the generation of ripples. Indeed, a recent observation of growth twins in a thin surface region of Ni (111) targets irradiated in the regime of HSFL formation provides a strong evidence of the role of the surface melting and resolidification in the generation of HSFLs, as the growth twinning can only occur in the course of the solidification [41]. The role of the transient melting and spallation in the generation of LSFLs, on the other hand, has recently been demonstrated by the observation of a relatively small depth of molten regions in the laser-structured Ni/Ti multi-layered samples, where the cores of the ripples are found to be spared of melting [38]. The analysis of subsurface microstructure of laser-processed targets also reveals an intriguing dependence on the crystallographic orientation of the irradiated surfaces [42, 43]. In particular, the LIPSS formation is found to be suppressed and the generation of subsurface crystal defects enhanced on (111)-oriented parts of a polycrystalline Ni surface, as compared to grains with (100) and (110) surface orientations [42]. The intricate role of electromagnetic and hydrodynamic mechanisms on HSFLs formation has recently been evidenced by the observation of self-arranged periodic nanovoids trapped under the surface as well as nanocavities at the surface [44]. Local nanocavitation process driven by near field enhancement was shown to be behind this deep sub-wavelength LIPSS formation. The results of recent depth-resolved chemical analysis of LIPSS generated on Ti surfaces reveal the formation of a relatively thick graded oxide layer [45], suggesting that laser-induced oxidation may be involved in the HSFL formation on reactive surfaces [37].

At higher laser fluences, in the spallation regime [46–48], the roughening of the surface generated by the first laser pulse may increase surface absorption and activate a feedback mechanism [7] driving the evolution of the initial random surface roughness towards the periodic ripples that maximize the laser energy absorption. The initial roughness generated by the first pulse, therefore, may play an important role in defining the LIPSS formation by subsequent repetitive laser irradiation. The characteristics of the nanoscale surface morphology generated by laser spallation are defined by a complex interplay of the laser-induced melting, nucleation and percolation of subsurface voids in the molten part of the target, formation of a transient foamy structure of liquid regions connecting the spalled layer with the bulk of the target [49], followed by breakup and rapid freezing of the transient liquid structures. The results of a recent large-scale molecular dynamics (MD) simulation of femtosecond laser spallation of a Ag target [50] demonstrate the ability of the atomistic modeling to provide detailed information on the mechanisms responsible for the formation of frozen surface nanospikes and their internal structure.

In this paper, we combine experimental characterization of HSFLs generated on monocrystalline Cr targets with surface orientation of (100) and (110) with a thorough computational analysis of the laser-induced spallation process based on a MD simulation of a (100) Cr target. The results of the joint study support a notion of a strong connection between the frozen surface morphology predicted in the simulation and the pulse-to-pulse evolution of surface roughness observed in the experiments. The spallation-induced roughness provides favorable conditions for positive feedback promoting the HSFLs formation. The dependence of the HSFLs formation on the crystal orientation is likely to be related to differences in the characteristics of surface morphology generated by the first laser pulse.

2 Experimental and computational methods

In this work, two monocrystalline samples having different surface orientations defined by Miller indexes (100) and (110) were irradiated. The two samples were first mechanically then electrolytically polished, which yields a surface roughness of about ~5 nm before irradiation. A Titanium-Sapphire femtosecond laser system (Legend Coherent, Inc.) operated at a central wavelength of 800 nm with a pulse duration of about 50 fs was used to irradiate Cr samples at a repetition rate of 1 kHz under atmospheric air pressure. Laser pulses were linearly polarized and attenuated through a pair of neutral density filters before being focused onto the sample surfaces through normal angle of incidence. Laser-induced surface modification was analyzed using a scanning electron microscope (SEM, FEI

NovananoSEM200) and an atomic force microscope (AFM, Agilent 5500).

The large-scale atomistic simulation aimed at revealing the processes responsible for the formation of surface roughness in the spallation irradiation regime are performed for a Cr target with (100) surface orientation irradiated by a 50 fs laser pulse at an absorbed fluence of 0.11 J/cm^2 , which is only $\sim 10\%$ above the spallation threshold. The simulation is performed with a hybrid atomistic–continuum model, which combines the atomistic MD representation of laser-induced structural and phase transformations with a continuum-level description of the electron sub-system based on the two-temperature model (TTM). A complete description of the combined TTM-MD model is provided in Refs. [47, 50, 51], whereas the parameterization of the model for Cr is described in Refs. [52, 53]. Below, we only provide a brief description of the computational setup used in the simulation reported in this paper.

The interatomic interactions between atoms in the MD part of the model are described by the embedded atom method (EAM) potential parametrized for Cr [53]. The potential provides a relatively accurate and computationally inexpensive description of Cr experimental properties, including lattice parameter, cohesive energy, elastic constants and their temperature dependence, melting temperature, and vacancy formation energy. To ensure a realistic representation of the spallation process and generation of nanoscale surface morphology, the simulation is performed for a large system (~ 126 million atoms) with lateral (parallel to irradiated surface) dimensions of $100 \times 100 \text{ nm}^2$ and the depth of the surface region of the target represented with atomic resolution equal to 150 nm. Periodic boundary conditions are applied along the lateral directions, and a free boundary condition is applied above the top surface of the target in order to simulate the uniaxial expansion and ejection of vapor atoms and liquid droplets during the ablation process. A pressure-transmission boundary condition [49, 53–55] is imposed at the bottom of the atomistic part of the system to preclude the reflection of the laser-induced pressure wave from the bottom of the MD computational cell. The TTM part of the model extends down to $1 \mu\text{m}$ to ensure the absence of any significant increase in the electron or lattice temperatures at the bottom of the computational domain by the end of the simulation. The thermophysical properties of Cr entering the TTM equations (electron-phonon coupling, electron heat capacity, and thermal conductivity) are described in Ref. [53]. Irradiation by a 50 fs laser pulse is represented through a source term added to the TTM equation for the electron temperature [51], with an optical penetration depth of 15 nm at a laser wavelength of 800 nm [56] assumed in the simulation.

3 Results and discussion

3.1 Laser induced periodic surface structures on Cr (100) surface

Since low spatial frequency LIPSS require a relatively high number of laser pulses to promote positive feedback, a Cr sample with (100) surface orientation has been irradiated with 30 pulses at an incident laser fluence of 0.3 J/cm^2 , which is below the single pulse phase explosion threshold. A complex arrangement of surface topography generated by the laser pulses can be seen in the SEM images shown in Fig. 1. Four types of LIPSS that differ by their orientation and periodicity can be distinguished in the images, namely, the far field perpendicular (FF_\perp), far field parallel (FF_\parallel), near field perpendicular (NF_\perp) and near field parallel (NF_\parallel), where the parallel and perpendicular refer to the ripple orientation with respect to the laser beam polarization. The origin of these structures and physical mechanisms leading to their formation can be ascribed to coherent interference between scattered waves and refracted near and far fields as evidenced by recent electromagnetic calculations [57]. In other words, different scattering conditions (near field enhancement, scattered far-field superposition, coherent superposition with incident beam, etc.) resulting from different local roughness can provoke different nanoscale rearrangements of material. However, several alternative approaches have been proposed in literature to explain the formation of such structures, including surface oxidation and high harmonic generation [37], laser induced surface plasma waves [40], and surface self-organization [31, 39]. In this work, we focus our attention on the NF_\parallel structures, since they appear upon exposure to a low energy dose and for a low number of laser pulses. In fact, for a high number of laser pulses, the concept of scattered wave becomes questionable. The analysis of the experimental observations for one or two laser pulses is addressing the onset of the LIPSS formation and allows for a more direct comparison with the results of modeling reported in Sect. 3.4.

3.2 Roughness triggering HSFLs formation in two pulse irradiation

The formation of NF_\parallel LIPSS is observed for a narrow range of laser fluences below the phase explosion threshold for single pulse irradiation. The structures discussed in this work are generated at an incident fluence of 0.3 J/cm^2 , which is defined as the “peak fluence” of the Gaussian laser pulse obtained by dividing the total optical energy by $\pi\omega/2$, where ω is the Gaussian beam waist [58]. The values

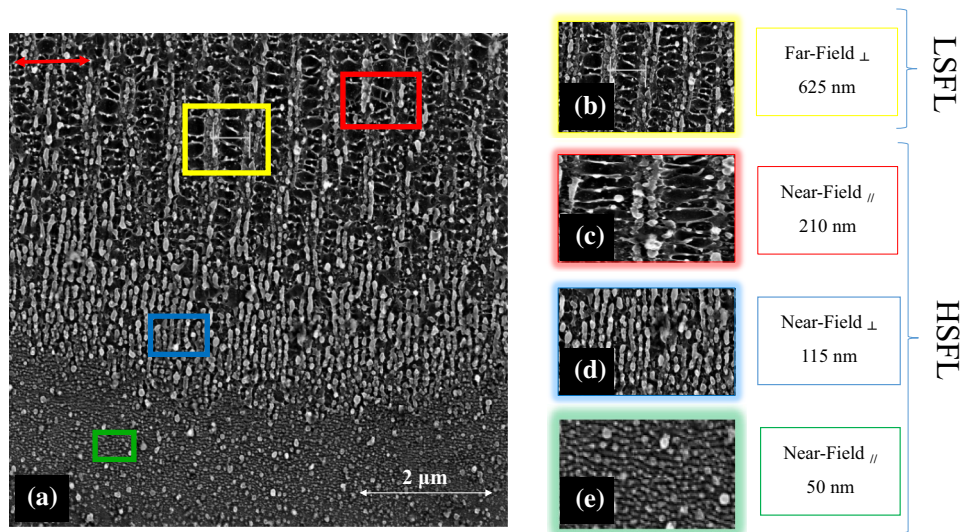


Fig. 1 SEM micrographs representing different types of LIPSS generated on (100) Cr target irradiated by 30 pulses at an incident laser fluence of 0.3 J/cm^2 , which is about 10% below the single pulse phase explosion threshold, F_{th} . **a** A large part of the laser spot where all types of LIPSS are present. **b** LSFL (FF_{\perp}) structures with period of $\sim 625 \text{ nm}$, close to laser wavelength. **c** HSFL (FF_{\parallel}) structures formed

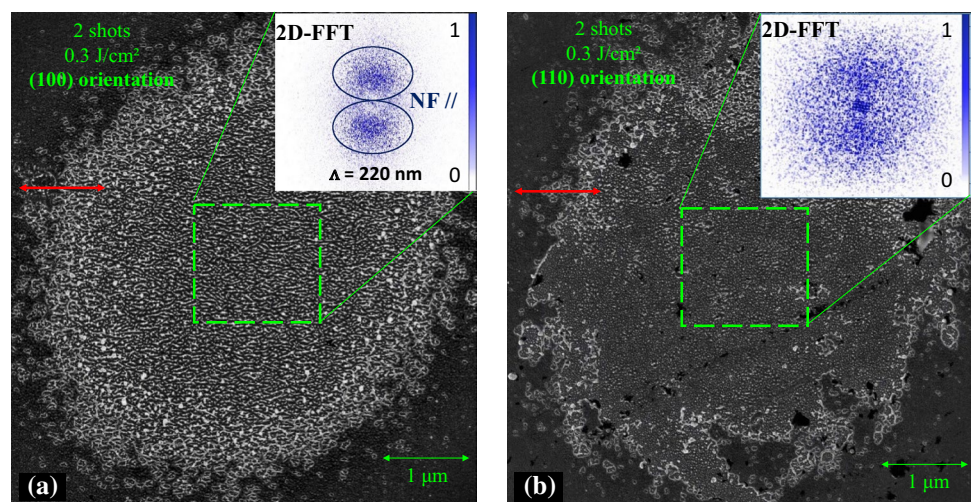
between LSFL structures. **d** HSFL (NF_{\perp}) structures formed on the periphery of LSFL. **e** HSFL (NF_{\parallel}) structures formed on the periphery of the spot, with periods much smaller than the laser wavelength. The direction of linear laser beam polarization is indicated by the red double arrow in the top left corner of **a**

of single pulse ablation threshold fluence, F_{th} , determined for two monocrystalline samples with different surface orientations are very similar to each other, 0.33 J/cm^2 for (100) and 0.32 J/cm^2 for (110) surfaces. Recent results of ab initio calculations reveal that the optical properties of Cr are not sensitive to the surface crystal orientation and do not exhibit large variation in the range of electron temperatures realized under irradiation conditions considered in this study [59]. The absorbed fluence, therefore, can be estimated using a constant value of reflectivity of Cr at 800 nm , $R = 0.55$ [56], which yields $\sim 0.13 \text{ J/cm}^2$ for the incident fluence of 0.3 J/cm^2 used in the experiments.

This value of the absorbed fluence is in the range between the spallation and phase explosion thresholds predicted in atomistic simulations performed for Cr targets [52], 0.10 and 0.28 J/cm^2 , respectively.

Laser induced surface modification generated on two targets with (100) and (110) surface orientation by irradiation with two laser pulses at an incident fluence of 0.3 J/cm^2 is analyzed in scanning electron microscope (SEM), with representative images shown in Fig. 2. The mere visual analysis of the SEM images suggests that elongated surface structures parallel to the direction of the laser beam parallelization are formed in the center of the laser spot on (100)

Fig. 2 SEM micrograph of Cr targets with **a** (100) surface orientation and **b** (110) surface orientation irradiated by 2 laser pulses at an incident fluence of 0.3 J/cm^2 , i.e., about 10% below the single pulse phase explosion threshold, F_{th} . The direction of linear laser beam polarization is indicated by the red double arrows. Insets in both images show FFT of the surface topography for regions outlined by the green dashed squares



surface, but are absent on (110) surface. To highlight this difference, the two-dimensional (2D) fast Fourier transform (FFT) amplitude was calculated for regions within the laser spots outlined by green dashed squares in Fig. 2. Two similar symmetric zones can be identified on the FFT plot shown as an inset in Fig. 2a for the laser-processed (100) surface, indicating the presence of $NF_{//}$ structures parallel to laser polarization with periodicity of about 220 nm. It is worth noting that for small number of pulses, i.e., under conditions of minimal feedback, the transient surface topography favors $NF_{//}$ structures exhibiting periodicities larger than those generated by multi-pulse feedback irradiation. For (110) surface, the FFT image shown in the inset of Fig. 2b exhibits a larger dispersion of the FFT peaks and reflects a much weaker tendency towards the HSFLs formation, as compared to (100) surface.

The strong dependence of the generation of $NF_{//}$ structures on the crystallographic surface orientation can be related to the hypothesis that the HSFLs result from superposition of waves scattered by roughness centers and implying local field enhancement [57, 60]. Most studies agree that surface roughness is necessary to initiate the LIPSS formation. Furthermore, a sufficiently rough surface is needed to support the excitement of a surface wave and to cause instability which gives rise to the structuring. To investigate the origin of the distinct propensities of targets with (100) and (110) surface orientations to the formation of $NF_{//}$ by two pulse laser irradiation, the information on surface roughening induced by the first laser pulse is needed and is discussed in the following section.

3.3 Surface roughness generated on (100) and (110) Cr targets by a single pulse irradiation

As discussed above, the formation of HSFLs is likely to be strongly affected by the shapes and size distribution of surface features generated by the first laser pulse. Thus, the surface roughness produced by a single laser pulse irradiation of (100) and (110) Cr targets is analyzed here for the same laser fluence (between the thresholds for spallation and phase explosion) that is used in the 30- and 2-pulse surface modification discussed in the previous sections. The surface topography in the centers of the laser-modified regions is characterized by the Atomic Force Microscope (AFM), and representative AFM micrographs are shown for the two targets in Fig. 3.

A statistical parameter that can be used to characterize the randomness of laser-generated surface roughness and sharpness of surface spikes is kurtosis (*sku*). This parameter is larger than 3 for “spiky” surfaces, lower than 3 for “bumpy” surfaces, and equal to 3 for completely random surface roughness. The more peaks a laser modified surface has, and the sharper the peaks are, the higher is the *sku*

value of the surface. The *sku* values evaluated for (100) and (110) surface orientations are 5.59 and 1.97, respectively. These values are consistent with qualitative observations one can make from the visual analysis of Fig. 3, where the fine nanoscale roughness observed for (100) surface is in a sharp contrast with a much coarser roughness of the (110) surface dominated by large bumps and flat-top mesas. Morphological features induced by the first pulse on the (100) orientation are connected by nanorims with length ranging from 10 to 16 nm, as shown in Fig. 3d. This important observation provides a strong support to the hypothesis that the spiky character of roughness generated by the first laser pulse irradiation of (100) surface plays a key role in the activation of the scattering mechanism leading to the formation of $NF_{//}$ structures, whereas a much smoother (110) surface emerging from the first pulse irradiation is less amenable to the HSFLs formation. To elucidate the physical mechanism responsible for the creation of the initial surface morphology by a single pulse laser irradiation, a large-scale atomistic simulation of laser interaction with a (100) Cr target is performed for irradiation conditions similar to those used in the experiments. The computational results are reported and discussed in the next section.

3.4 Large-scale atomistic simulation of laser spallation

The general mechanisms responsible for the material ejection in regime of photomechanical spallation has been studied in a number of earlier computational studies, e.g., [46, 47, 49, 50, 52, 55, 61–64], although the analysis of surface morphology produced by the spallation process has been hampered by the short length- and time-scales of most of the atomistic simulations reported so far. Here, we first briefly review the mechanisms of the laser spallation and then focus on the analysis of the surface morphology enabled by the relatively large scale of the simulation reported in this paper.

The thermodynamic conditions leading to laser spallation are illustrated by the contour plots of the spatial and temporal evolution of density, temperature, and pressure in the surface region of the irradiated target shown in Fig. 4. The black lines in the contour plots separate the transiently melted surface region from the crystalline part of the target. The laser excitation of the conduction band electrons is followed by fast electron-phonon equilibration and leads to a rapid increase of the lattice temperature in the surface region of the target from 300 to ~3700 K during the first 5 ps after the laser pulse, Fig. 4b. The rapid heating causes prompt homogeneous melting of a 36-nm-deep surface region of the target superheated above the limit of crystal stability [51, 65, 66]. The laser energy deposition and equilibration occur under conditions of the so-called inertial stress confinement, i.e., on a timescale that is shorter than the time required for

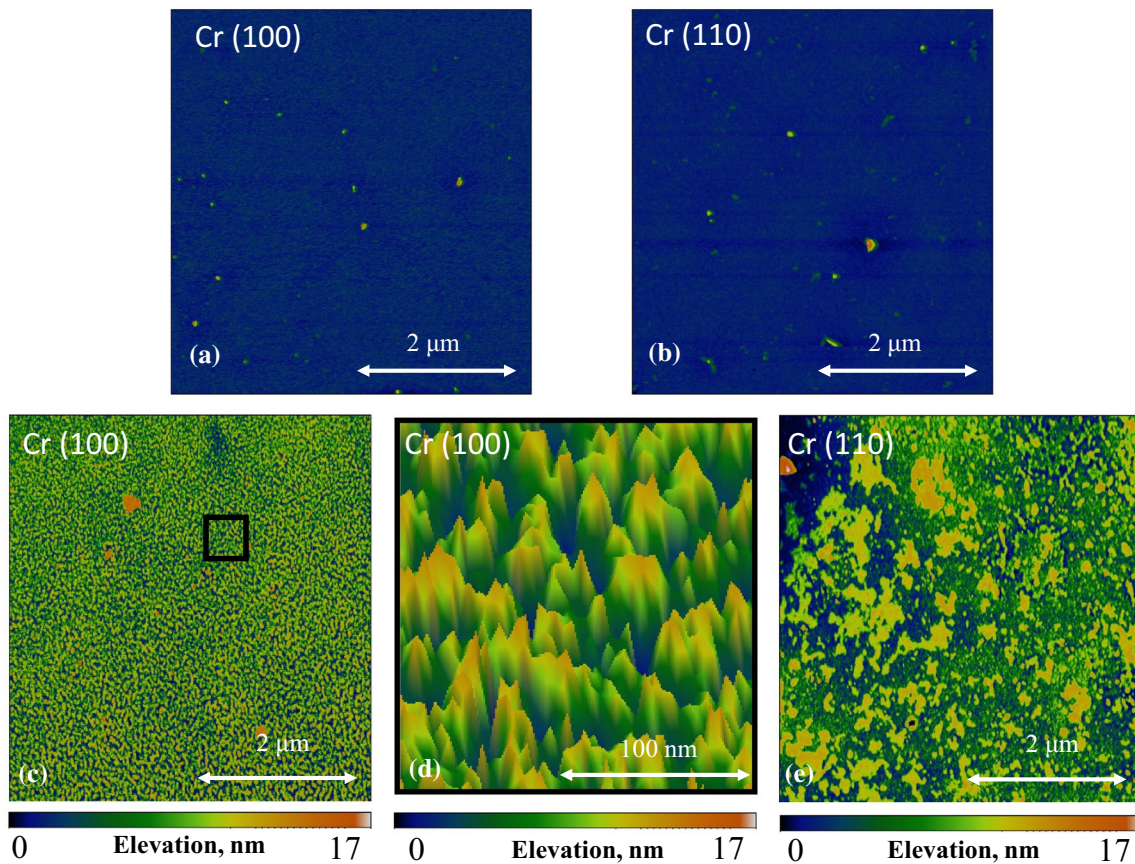


Fig. 3 AFM micrographs of Cr targets before and after single pulse laser irradiation. **a, b** Targets with (100) and (110) surface orientations before laser irradiation. **c** Target with (100) surface orientation irradiated at an incident fluence of 0.3 J/cm^2 , i.e., about 10% below

the single pulse phase explosion threshold, F_{th} . **d** 3D view of surface topography shown for a region outlined by the black square in **c**. **e** Target with (110) surface orientation irradiated under similar conditions as in **c**

the mechanical relaxation (expansion) of the heated surface region [46, 48]. The almost constant-volume heating results in the generation of compressive stresses, while the interaction of the laser-induced compressive stresses with the free surface of the irradiated target produces a tensile component of the stress wave propagating into the bulk of the target, as can be seen from the pressure contour plot in Fig. 4c. At a certain depth under the surface, the tensile stress exceeds the dynamic strength of the molten material and leads to the nucleation and growth of subsurface voids in a process that is commonly called the laser-induced cavitation or spallation [44, 46, 67]. The appearance of voids is reflected in the density contour plot shown in Fig. 4a, where the reduction of density is first observed at about 30 ps after the laser pulse. The low-density region expands with time, as the voids grow, coalesce, percolate, and eventually produce an array of elongated liquid bridges that connect the bulk of the target to a top molten layer accelerated in the direction away from the target by the initial relaxation of laser-induced stresses.

The extension of the liquid bridges hardly decelerates the top layer that continues to move away from the target at an almost constant velocity of $\sim 180 \text{ m/s}$. The elongation of the liquid bridges proceeds simultaneously with solidification of lower parts of the bridges adjacent to the target, as evidenced by the extension of the black line marking the location of the solidification front in Fig. 4 into the low-density region that corresponds to the liquid bridges. The upward motion of the molten layer leads to eventual breakup of the liquid bridges and complete separation of the layer from the target by $\sim 750 \text{ ps}$.

The visual picture of the processes described above is provided by a series of snapshots of atomic configurations taken at different times in the course of the simulation and shown in Fig. 5. The snapshots illustrate the appearance of a large number of voids in the molten part of the target by 50 ps, the evolution of the cavitation region into a “forest” of liquid bridges by 200 ps, and the breakup of the bridges upon further upward motion of the top molten layer. Only

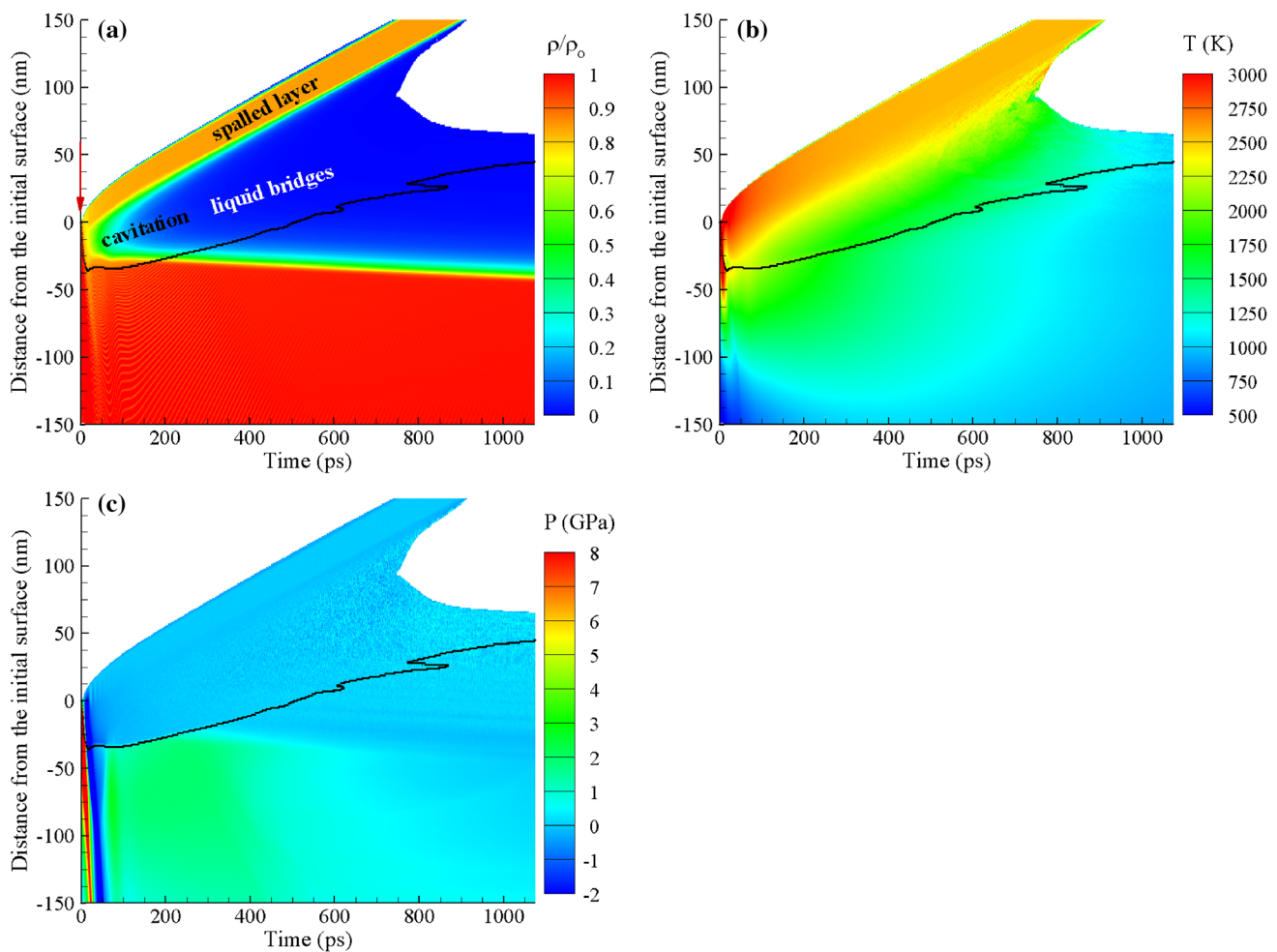


Fig. 4 Contour plots of the spatial and temporal evolution of **a** density, **b** temperature, and **c** pressure, in a large-scale TTM-MD simulation of a bulk (001) Cr target irradiated by a 50 fs laser pulse at an absorbed laser fluence of 0.11 J/cm^2 , $\sim 10\%$ above the spallation threshold. The laser pulse is directed along the Y -axis as shown by the

red arrow in **a**. The black line separates the melted region from the crystalline part of the Cr target. The visual picture of the subsurface "cavitation" region evolving into an array of "liquid bridges" connecting the "spalled layer" with the rest of the target can be seen in Fig. 5

a small number of gas-phase atoms can be seen inside the growing subsurface voids, thus providing further evidence for the photomechanical nature of the cavitation/spallation process, i.e., the driving force for the nucleation and growth of the voids is the relaxation of the laser-induced stresses rather than the vapor pressure in the boiling process.

In contrast to the smaller-scale simulations, where the voids quickly "outgrow" the lateral size of the computational cell and self-interact to promote a prompt separation of the top liquid layer shortly after the void nucleation, e.g., [46, 51, 62, 63], the evolution of voids illustrated in Fig. 5 takes longer time and proceeds through the formation of a transient foamy structure of interconnected liquid bridges connecting the upper 27-nm-thick liquid layer with the rest of the target. The size of the largest elongated void and the distances between the liquid bridges are substantially smaller

than the lateral size of the computational cell, suggesting that the size effects and the periodic boundary conditions are not introducing any major artifacts into the dynamics of the spallation process. This enables us to continue the simulation until the time of complete resolidification of the surface region and to perform analysis of the final surface morphology generated in the spallation process, which is reported in the next section.

3.5 Surface roughness generated in the spallation process

The nanoscale surface morphology generated in the spallation process is illustrated in Fig. 6a,b, where a side and a top views of the surface structure are shown for a time of 1056 ps, when eight out of nine surface spikes produced via

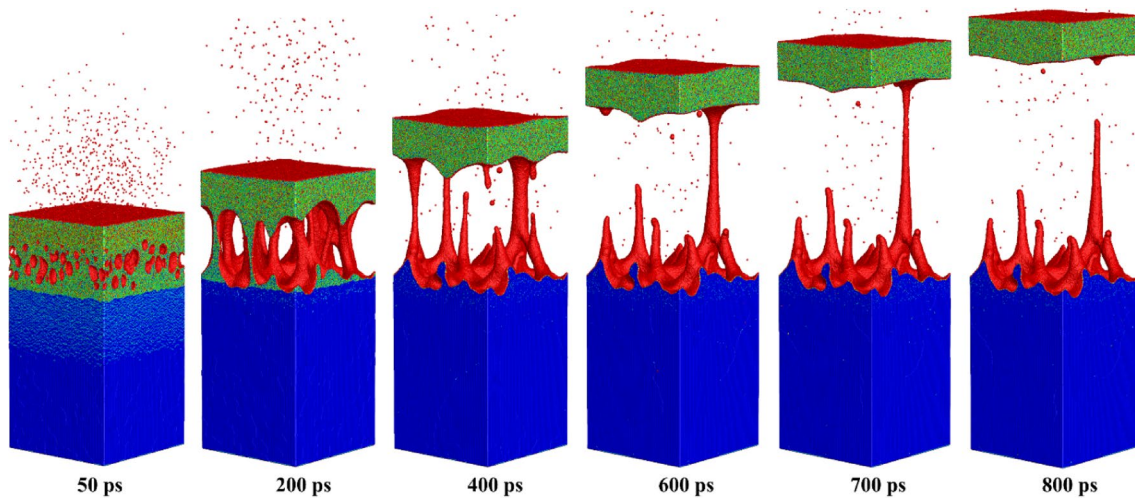


Fig. 5 Snapshots of atomic configurations obtained in a TTM-MD simulation of laser spallation of a bulk (001) Cr target irradiated with a 50 fs laser pulse at an absorbed laser fluence of 0.11 J/cm^2 . The laser pulse is directed from the top of the images. The atoms are colored according to their potential energies: the dark blue regions represent the bcc Cr structure, green regions correspond to the molten Cr, and the atoms at the top surface of the target and at the internal

surfaces appearing in the spallation process are colored red. The light blue stripes that can be seen in the crystalline part of Cr target at 50 ps and disappear at later time represent the unstable stacking faults [53] transiently appearing in the system in response to the uniaxial expansion caused by the dynamic relaxation of the laser-induced stresses

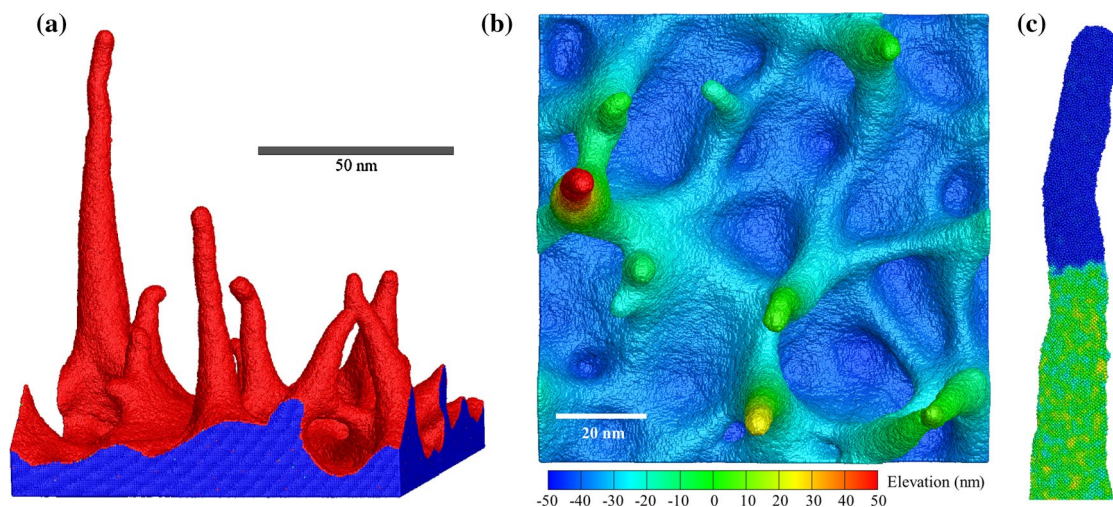


Fig. 6 Side (a) and top (b) views of the frozen surface morphology generated in a TTM-MD simulation of laser-induced photomechanical spallation of a bulk (001) Cr target irradiated with a 50 fs laser pulse at an absorbed laser fluence of 0.11 J/cm^2 . The $100 \times 100 \text{ nm}^2$ surface region features nine solidified spikes with length ranging from 12 to 110 nm. An enlarged view of a top 40 nm part of the tallest spike is shown in c. The atoms in a are colored according to their

potential energies with the same coloring scale as in Fig. 5. In b, the atoms are colored according to their elevation with respect to the initial level of the surface. In c, the atoms are colored by the local-order parameter, so that the lower crystalline part (green) could be clearly distinguished from the top part that remains in the disordered state (blue)

the spallation and breakup of the liquid bridges are already completely crystallized. The characteristic morphological features present on the surface include nine spikes with the length ranging between 12 and 110 nm, nanocavities, nanoprotusions, and nanorims connecting the spikes and

outlining the nanocavities. Several small subsurface voids are also present at the base of some of the frozen spikes (not visible in Fig. 6 but revealed in the detailed analysis of the resolidified targets). Eight out of the nine spikes are fully crystallized through the rapid propagation of the

crystal-liquid interface from the bulk of the single crystal target. The crystallization front accelerates with increasing undercooling, reaches its maximum velocity of ~ 150 m/s at a temperature of about $0.75T_m$, and then slows down as the temperature continues to drop further after the separation of the spalled layer from the liquid bridges. By the time of 1056 ps, for which the images are shown in Fig. 6, only the top 20 nm part of the tallest spike remains disordered, as can be seen from the enlarged view of the tip of the spike in Fig. 6c. The atoms in Fig. 6c are colored by the local-order parameter [51], so that the front of the epitaxial crystallization could be clearly identified. The crystallization front is still moving upwards, and one can expect complete crystallization of the spike within the next nanosecond. Note that despite the disordered structure of the tip of the tallest spike, its shape does not undergo any significant changes following the formation of the spike through the breakup of the liquid bridge (compare snapshot for 800 ps in Fig. 5 with Fig. 6a). This observation can be related to the rapid drop of the temperature of the spike (and corresponding increase in viscosity), which is already as low as $0.45T_m$ at the end of the simulation.

The surface morphology predicted by the TTM-MD simulation of laser spallation of Cr target is consistent with the results of experimental imaging of nanoscale surface roughness produced in femtosecond laser processing of different metals, e.g., Cu [68, 69], Au [70], Ag [71], and W [72]. The surface structures observed in the experiments feature elongated frozen nanopikes, nanorims and nanocavities, which are very similar to the simulated surface morphology shown in Fig. 6. The characteristic sizes of the surface features, however, are sensitive to the properties of target material and irradiation conditions (number of laser pulses and relative magnitude of the laser fluence with respect to the spallation threshold), thus hindering the establishment of direct quantitative links between the computational predictions and the experimental data. The coordinated computational-experimental study of Cr targets irradiated in the same spallation regime, reported in this work, provides an opportunity to bring the connection between the modeling predictions and experimental observations to the quantitative level. In particular, the inspection of the AFM image shown for Cr (100) surface in Fig. 3c,d indicates that several frozen spikes with heights exceeding 10 nm are present on an area with dimensions of 100×100 nm², which is in a good agreement with the surface morphology shown for the same surface area in Fig. 6b.

A number of possible explanations have been suggested in literature for the formation of surface nanostructures on metal surfaces irradiated by femtosecond laser pulses. A possible spatial variation of the absorbed laser energy (due to the inhomogeneity of the incident laser beam, the enhanced

absorption by surface defects, or the interference of the incident laser light with surface scattered waves), leading to the formation of localized nanoscale melted regions and redistribution/expulsion of the molten material driven by the temperature gradients is suggested as the origin of nanoscale surface morphology in Ref. [68]. The possible role of heterogeneous melting of the irradiated surface is discussed in Ref. [72], while the relaxation of laser-induced stresses and spallation are highlighted in the analysis reported in Refs. [69, 71].

The results of the simulation presented in this paper provide a convincing evidence in favor of the scenario where the nanoscale surface roughness appears as a result of spallation proceeding simultaneously with rapid resolidification of the transiently melted surface region of the target. The generation, coarsening, and percolation of subsurface voids in the molten part of the target lead to the formation of liquid bridges and vertical walls separating the voids, see, e.g., a snapshot for 200 ps in Fig. 5. As the top molten layer moves away from the target, the liquid walls and bridges break up and retract due to the action of the surface tension. The breakup of the liquid bridges, however, proceeds simultaneously with the advancement of solidification front from the bulk of the target, which captures and freezes the transient liquid structures generated in the dynamic spallation process. Actually, the solidification front reaches the base of the liquid bridges as early as ~ 200 ps, as manifested by the black line entering the low-density region in Fig. 4a and the blue (crystalline) region extending into the bridges by 400 ps in Fig. 5. By the time the liquid bridges break up and the spalled layer separates from the target (~ 750 ps), some of the smaller nanopikes are already completely solidified and only the longest ones remain partially melted. The competition of the evolution of the shapes of the liquid parts of the spikes driven by the minimization of the surface energy with the rapid solidification is defining the final shapes of the nanopikes. In particular, the bent shapes of the nanopikes clearly visible in Fig. 6a, as well as spherical “heads” that would form if the solidification would be slightly slower, are commonly observed in the experimental images [68–70, 72]. Note that in addition to the advancement of the solidification front from the bulk of the target observed as the only solidification mechanism in the simulation reported in this paper, an additional contribution from the homogeneous nucleation of new crystallites is possible if a sufficiently strong undercooling is reached in the liquid parts of the nanopikes, as has been demonstrated for Ag in Ref. [50].

The mechanistic insights into the formation of frozen surface features obtained in the simulation of laser spallation of a (100) Cr target also provide a hint to the possible explanation of the strong dependence of the surface topography on the crystallographic orientation of the irradiated

surface. The velocity of crystallization front propagation is faster for (100) crystal-liquid interface as compared to more densely packed (111) or (110) interfaces [73], while the optical absorption, melting depth, and magnitude of the laser-induced pressure wave are not expected to exhibit a strong orientational dependence. The slower solidification front propagation for the densely packed interfaces leaves more time for the surface tension to smooth out the molten surface features generated by the breakup of the liquid bridges to the spalled layer.

4 Summary

The physical mechanisms responsible for the formation of HSFLs in femtosecond laser interactions with metal surfaces are investigated in a joint experimental and computational study that combines a detailed analysis of surface morphology produced by 30, 2, and 1 pulse irradiation of monocrystalline Cr samples with a large-scale molecular dynamics simulation of laser interaction with a Cr target performed in the same irradiation regime. The electron and atomic force microscopy analysis of the irradiated surfaces reveals that the material response to the first laser pulse is strongly dependent on crystallographic surface orientation, with (100) Cr surface exhibiting the formation of higher and more refined nanoscale surface roughness as compared to (110) surface. The higher surface roughness generated by the first laser pulse activates scattering of the laser light and the local field enhancement upon irradiation by the second laser pulse, leading to the formation of much more pronounced high spatial frequency structures on the (100) surface as compared to (110) one. When applying additional laser pulses, different types of periodic surface structures start to emerge due to the interference between the incident laser light and waves scattered by roughness centers strengthening specific periodicities by positive feedback. The appearance of the periodic surface structures, therefore, can be traced back to the initial surface roughness generated by the first laser pulse.

To reveal the processes responsible for the formation of the surface roughness by single pulse laser irradiation, a large-scale atomistic simulation is performed for a (100) Cr target irradiated in the spallation regime. The simulation provides a detailed picture of the spallation process driven by the relaxation of the laser-induced stresses and leading to the formation of complex nanoscale surface roughness featuring elongated frozen nanospikes, nanorims and nanocavities with dimensions similar to those observed experimentally. The results of the simulation suggest that the characteristics of nanoscale surface morphology are defined by the competition between the evolution of transient liquid structures generated in the spallation process and the rapid

resolidification of the surface region of the target. The strong dependence of the surface topography produced in single pulse irradiation experiments on the crystallographic orientation of target surface may be related to the anisotropy of the crystallization front propagation, which provides more time for the relaxation of molten surfaces when the solidification process is slower. The connection between the initial nanoscale roughness generated by the first laser pulse and the subsequent formation of periodic surface structures, established in the present study, contributes to the progress towards the general goal of untangling the complex multi-scale phenomenon of the LIPSS formation.

Acknowledgements This work was supported by the LABEX MANUTECH-SISE (ANR-10-LABX-0075) of Université de Lyon, within the program “Investissements d’Avenir” (ANR-11-IDEX-0007) operated by the French National Research Agency (ANR). Financial support for the computational part of this work was provided by the National Science Foundation (NSF) through Grant DMR-1610936. Computational support was provided by the NSF through the Extreme Science and Engineering Discovery Environment (project TGDMR110090) and the Oak Ridge Leadership Computing Facility (INCITE project MAT130).

References

1. A. Cunha, A.P. Serro, V. Oliveira, A. Almeida, R. Vilar, M.-C. Durrieu, Wetting behaviour of femtosecond laser textured Ti-6Al-4V surfaces. *Appl. Surf. Sci.* **265**, 688 (2013)
2. F.F. Dave, C. Hae Woon, Z. Burr, K.S. Jeremy, J.C. Jeffery, V.O. Susan, L.J. Lee, Femtosecond laser micromachining of dielectric materials for biomedical applications. *J. Micromech. Microeng.* **18**, 035020 (2008)
3. J. Krüger, W. Kautek, M. Lenzner, S. Sartania, C. Spielmann, F. Krausz, Laser micromachining of barium aluminium borosilicate glass with pulse durations between 20 fs and 3 ps. *Appl. Surf. Sci.* **127–129**, 892 (1998)
4. S. Nolte, C. Momma, H. Jacobs, A. Tünnermann, B.N. Chichkov, B. Wellegehausen, H. Welling, Ablation of metals by ultrashort laser pulses. *J. Opt. Soc. Am. B* **14**, 2716 (1997)
5. R. Le Harzic, N. Huot, E. Audouard, C. Jonin, P. Laporte, S. Vallette, A. Fraczkiewicz, R. Fortunier, Comparison of heat affected zone due to nanosecond and femtosecond laser pulses using transmission electronic microscopy. *Appl. Phys. Lett.* **80**, 3886 (2002)
6. V. Margetic, K. Niemax, R. Hergenröder, Application of femtosecond laser ablation time-of-flight mass spectrometry to in-depth multilayer analysis. *Anal. Chem.* **75**, 3435 (2003)
7. M.J. Abere, M. Zhong, J. Krüger, J. Bonse, Ultrafast laser-induced morphological transformations. *MRS Bull.* **41**, 969 (2016)
8. R. Buividas, M. Mikutis, S. Juodkazis, Surface and bulk structuring of materials by ripples with long and short laser pulses: recent advances. *Prog. Quantum Electron.* **38**, 119 (2014)
9. L. Romoli, C.A.A. Rashed, G. Lovicu, G. Dini, F. Tantussi, F. Fuso, M. Fiaschi, Ultrashort pulsed laser drilling and surface structuring of microholes in stainless steels. *CIRP Ann. Manuf. Technol.* **63**, 229 (2014)
10. R.V. Volkov, D.M. Golishnikov, V.M. Gordienko, A.B. Savel'ev, Overheated plasma at the surface of a target with a periodic

- structure induced by femtosecond laser radiation. *JETP Lett.* **77**, 473 (2003)
11. A.Y. Vorobyev, V.S. Makin, C. Guo, Brighter light sources from black metal: significant increase in emission efficiency of incandescent light sources. *Phys. Rev. Lett.* **102**, 234301 (2009)
 12. O. Raimbault, S. Benayoun, K. Anselme, C. Mauclair, T. Bourgade, A.M. Kietzig, P.L. Girard-Lauriault, S. Valette, C. Donnet, The effects of femtosecond laser-textured Ti-6Al-4V on wettability and cell response. *Mater. Sci. Eng. C* **69**, 311 (2016)
 13. M.S. Ahsan, F. Ahmed, Y.G. Kim, M.S. Lee, M.B.G. Jun, Colorizing stainless steel surface by femtosecond laser induced micro/nano-structures. *Appl. Surf. Sci.* **257**, 7771 (2011)
 14. B. Dusser, Z. Sagan, H. Soder, N. Faure, J.P. Colombier, M. Jourlin, E. Audouard, Controlled nanostructures formation by ultra fast laser pulses for color marking. *Opt. Express* **18**, 2913 (2010)
 15. A.A. Ionin, S.I. Kudryashov, S.V. Makarov, L.V. Seleznev, D.V. Sinityn, E.V. Golosov, O.A. Golosova, Y.R. Kolobov, A.E. Ligachev, Femtosecond laser color marking of metal and semiconductor surfaces. *Appl. Phys. A* **107**, 301 (2012)
 16. G. Li, J. Li, Y. Hu, C. Zhang, X. Li, J. Chu, W. Huang, Femtosecond laser color marking stainless steel surface with different wavelengths. *Appl. Phys. A* **118**, 1189 (2014)
 17. J. Yao, C. Zhang, H. Liu, Q. Dai, L. Wu, S. Lan, A.V. Gopal, V.A. Trofimov, T.M. Lysak, Selective appearance of several laser-induced periodic surface structure patterns on a metal surface using structural colors produced by femtosecond laser pulses. *Appl. Surf. Sci.* **258**, 7625 (2012)
 18. J.R. Bush, B.K. Nayak, L.S. Nair, M.C. Gupta, C.T. Laurencin, Improved bio-implant using ultrafast laser induced self-assembled nanotexture in titanium. *J. Biomed. Mater. Res. B* **97 B**, 299 (2011)
 19. A. Cunha, A.-M. Elie, L. Plawinski, A.P. Serro, A.M. Botelho do Rego, A. Almeida, M.C. Urdaci, M.-C. Durrieu, R. Vilar, Femtosecond laser surface texturing of titanium as a method to reduce the adhesion of *Staphylococcus aureus* and biofilm formation. *Appl. Surf. Sci.* **360**, 485 (2016)
 20. V. Dumas, A. Guignandon, L. Vico, C. Mauclair, X. Zapata, M.T. Linossier, W. Boulefour, J. Granier, S. Peyroche, J.C. Dumas, H. Zahouani, A. Rattner, Femtosecond laser nano/micro patterning of titanium influences mesenchymal stem cell adhesion and commitment. *Biomed. Mater.* **10**, 055002 (2015)
 21. J.J. Yu, Y.F. Lu, Laser-induced ripple structures on Ni-P substrates. *Appl. Surf. Sci.* **148**, 248 (1999)
 22. N. Yasumaru, K. Miyazaki, J. Kiuchi, E. Sentoku, Control of tribological properties of diamond-like carbon films with femtosecond-laser-induced nanostructuring. *Diam. Relat. Mater.* **20**, 542 (2011)
 23. N. Yasumaru, K. Miyazaki, J. Kiuchi, Frictional properties of diamond-like carbon, glassy carbon and nitrides with femtosecond-laser-induced nanostructure. *Appl. Surf. Sci.* **254**, 2364 (2008)
 24. M. Pfeiffer, A. Engel, H. Gruettner, K. Guenther, F. Marquardt, G. Reisse, S. Weissmantel, Ripple formation in various metals and super-hard tetrahedral amorphous carbon films in consequence of femtosecond laser irradiation. *Appl. Phys. A* **110**, 655 (2013)
 25. A. Mizuno, T. Honda, J. Kikuchi, Y. Iwai, N. Yasumaru, K. Miyazaki, Friction properties of the DLC film with periodic structures in nano-scale. *Tribol. Online* **1**, 44 (2006)
 26. E. Rebollar, M. Castillejo, T.A. Ezquerro, Laser induced periodic surface structures on polymer films: from fundamentals to applications. *Eur. Polym. J.* **73**, 162 (2015)
 27. H.W. Chang, Y.C. Tsai, C.W. Cheng, C.Y. Lin, Y.W. Lin, T.M. Wu, Nanostructured Ag surface fabricated by femtosecond laser for surface-enhanced Raman scattering. *J. Colloid Interface Sci.* **360**, 305 (2011)
 28. R. Buividas, P.R. Stoddart, S. Juodkazis, Laser fabricated ripple substrates for surface-enhanced Raman scattering. *Ann. Phys.* **524**, L5 (2012)
 29. J.E. Sipe, J.F. Young, J.S. Preston, H.M. Van Driel, Laser-induced periodic surface structure. *Phys. Rev. B* **27**, 1141 (1983)
 30. M. Hashida, Y. Miyasaka, Y. Ikuta, S. Tokita, S. Sakabe, Crystal structures on a copper thin film with a surface of periodic self-organized nanostructures induced by femtosecond laser pulses. *Phys. Rev. B* **83**, 235413 (2011)
 31. J. Reif, F. Costache, O. Varlamova, G. Jia, M. Ratzke, Self-organized regular surface patterning by pulsed laser ablation. *Phys. Status Solidi* **6**, 681 (2009)
 32. C. Xie, X. Li, K. Liu, M. Zhu, R. Qiu, Q. Zhou, Direct writing of sub-wavelength ripples on silicon using femtosecond laser at high repetition rate. *Appl. Surf. Sci.* **360**, 896 (2016)
 33. S. Höhm, M. Herzlieb, A. Rosenfeld, J. Krüger, J. Bonse, Dynamics of the formation of laser-induced periodic surface structures (LIPSS) upon femtosecond two-color double-pulse irradiation of metals, semiconductors, and dielectrics. *Appl. Surf. Sci.* **374**, 331 (2016)
 34. J. Cui, A. Nogales, T.A. Ezquerro, E. Rebollar, Influence of substrate and film thickness on polymer LIPSS formation. *Appl. Surf. Sci.* **394**, 125 (2017)
 35. M.H. Dar, R. Kuladeep, V. Saikiran, N.D. Rao, Femtosecond laser nanostructuring of titanium metal towards fabrication of low-reflective surfaces over broad wavelength range. *Appl. Surf. Sci.* **371**, 479 (2016)
 36. R. Le Harzic, D. Dörr, D. Sauer, M. Neumeier, M. Epple, H. Zimmermann, F. Stracke, Formation of periodic nanoripples on silicon and germanium induced by femtosecond laser pulses. *Phys. Procedia* **12**, 29 (2011)
 37. X.-F. Li, C.-Y. Zhang, H. Li, Q.-F. Dai, S. Lan, S.-L. Tie, Formation of 100-nm periodic structures on a titanium surface by exploiting the oxidation and third harmonic generation induced by femtosecond laser pulses. *Opt. Express* **22**, 28086 (2014)
 38. L.T. Canguero, A.J. Cavaleiro, J. Morgiel, R. Vilar, Mechanisms of the formation of low spatial frequency LIPSS on Ni/Ti reactive multilayers. *J. Phys. D.* **49**, 36 (2016)
 39. S. Sakabe, M. Hashida, S. Tokita, S. Namba, K. Okamuro, Mechanism for self-formation of periodic grating structures on a metal surface by a femtosecond laser pulse. *Phys. Rev. B* **79**, 033409 (2009)
 40. G.D. Tsididis, C. Fotakis, E. Stratakis, From ripples to spikes: a hydrodynamical mechanism to interpret femtosecond laser-induced self-assembled structures. *Phys. Rev. B* **92**, 041405 (2015)
 41. X. Sedao, M.V. Shugaev, C. Wu, T. Douillard, C. Esnouf, C. Maurice, S. Reynaud, F. Pigeon, F. Garrelie, L.V. Zhigilei, J.-P. Colombier, Growth twinning and generation of high-frequency surface nanostructures in ultrafast laser-induced transient melting and resolidification. *ACS Nano* **10**, 6995 (2016)
 42. X. Sedao, C. Maurice, F. Garrelie, J.-P. Colombier, S. Reynaud, R. Quey, F. Pigeon, Influence of crystal orientation on the formation of femtosecond laser-induced periodic surface structures and lattice defects accumulation. *Appl. Phys. Lett.* **104**, 171605 (2014)
 43. X. Sedao, C. Maurice, F. Garrelie, J.P. Colombier, S. Reynaud, R. Quey, G. Blanc, F. Pigeon, Electron backscatter diffraction characterization of laser-induced periodic surface structures on nickel surface. *Appl. Surf. Sci.* **302**, 114 (2014)
 44. X. Sedao, A. Abou Saleh, A. Rudenko, T. Douillard, C. Esnouf, S. Reynaud, C. Maurice, F. Pigeon, F. Garrelie, J.P. Colombier, Self-arranged periodic nanovoids by ultrafast laser-induced near-field enhancement. *ACS Photonics* (2018). <https://doi.org/10.1021/acsp Photonics.7b01438>

45. S.V. Kirner, T. Wirth, H. Sturm, J. Krüger, J. Bonse, Nanometer-resolved chemical analyses of femtosecond laser-induced periodic surface structures on titanium. *J. Appl. Phys.* **122**, 104901 (2017)
46. E. Leveugle, D.S. Ivanov, L.V. Zhigilei, Photomechanical spallation of molecular and metal targets: molecular dynamics study. *Appl. Phys. A* **79**, 1643 (2004)
47. L.V. Zhigilei, Z. Lin, D.S. Ivanov, Atomistic modeling of short pulse laser ablation of metals: connections between melting, spallation, and phase explosion. *J. Phys. Chem. C* **113**, 11892 (2009)
48. G. Paltauf, P.E. Dyer, Photomechanical processes and effects in ablation. *Chem. Rev.* **103**, 487 (2003)
49. C. Wu, L.V. Zhigilei, Microscopic mechanisms of laser spallation and ablation of metal targets from large-scale molecular dynamics simulations. *Appl. Phys. A* **114**, 11 (2014)
50. C. Wu, L.V. Zhigilei, Nanocrystalline and polyicosahedral structure of a nanospire generated on metal surface irradiated by a single femtosecond laser pulse. *J. Phys. Chem. C* **120**, 4438 (2016)
51. D.S. Ivanov, L.V. Zhigilei, Combined atomistic-continuum modeling of short-pulse laser melting and disintegration of metal films. *Phys. Rev. B* **68**, 064114 (2003)
52. E.T. Karim, Z. Lin, L.V. Zhigilei, Molecular dynamics study of femtosecond laser interactions with Cr targets. In: *AIP Conference Proceedings*. vol. 1464, p. 280, (2012)
53. Z. Lin, R.A. Johnson, L.V. Zhigilei, Computational study of the generation of crystal defects in a bcc metal target irradiated by short laser pulses. *Phys. Rev. B* **77**, 214108 (2008)
54. L.V. Zhigilei, B.J. Garrison, Pressure waves in microscopic simulations of laser ablation. In: *Materials Research Society Symposia Proceedings*, vol. 538, p. 491 (1999)
55. L.V. Zhigilei, B.J. Garrison, Microscopic mechanisms of laser ablation of organic solids in the thermal and stress confinement irradiation regimes. *J. Appl. Phys.* **88**, 1281 (2000)
56. E.D. Palik (ed.), *Handbook of Optical Constants of Solids* (Academic Press, 1997)
57. H. Zhang, J.P. Colombier, C. Li, N. Faure, G. Cheng, R. Stoian, Coherence in ultrafast laser-induced periodic surface structures. *Phys. Rev. B* **92**, 17 (2015)
58. J.M. Liu, Simple technique for measurements of pulsed Gaussian-beam spot sizes. *Opt. Lett.* **7**, 196 (1982)
59. E. Bevilion, R. Stoian, J.P. Colombier, submitted, (2018)
60. A. Rudenko, J.-P. Colombier, S. Höhm, A. Rosenfeld, J. Krüger, J. Bonse, T.E. Itina, Spontaneous periodic ordering on the surface and in the bulk of dielectrics irradiated by ultrafast laser: a shared electromagnetic origin. *Sci. Rep.* **7**, (2017)
61. B.J. Demaske, V.V. Zhakhovskiy, N.A. Inogamov, I.I. Oleynik, Ablation and spallation of gold films irradiated by ultrashort laser pulses. *Phys. Rev. B* **82**, 064113 (2010)
62. P. Lorazo, L.J. Lewis, M. Meunier, Thermodynamic pathways to melting, ablation, and solidification in absorbing solids under pulsed laser irradiation. *Phys. Rev. B* **73**, 134108 (2006)
63. H.Y. Lai, P.H. Huang, Laser-irradiated thermodynamic behaviors of spallation and recombination at solid-state interface. *Appl. Surf. Sci.* **254**, 3067 (2008)
64. S.I. Anisimov, V.V. Zhakhovskii, N.A. Inogamov, K. Nishihara, A.M. Oparin, Y.V. Petrov, Destruction of a solid film under the action of ultrashort laser pulse. *JETP Lett.* **77**, 606 (2003)
65. Z. Lin, E. Leveugle, E.M. Bringa, L.V. Zhigilei, Molecular dynamics simulation of laser melting of nanocrystalline Au. *J. Phys. Chem. C* **114**, 5686 (2010)
66. S.N. Luo, T.J. Ahrens, T. Çağın, A. Strachan, W.A. Goddard, D.C. Swift, Maximum superheating and undercooling: systematics, molecular dynamics simulations, and dynamic experiments. *Phys. Rev. B* **68**, 134206 (2003)
67. M.V. Shugaev, C. Wu, O. Armbruster, A. Naghilou, N. Brouwer, D.S. Ivanov, T.J.Y. Derrien, N.M. Bulgakova, W. Kautek, B. Rethfeld, L.V. Zhigilei, Fundamentals of ultrafast laser-material interaction. *MRS Bull.* **41**, 960 (2016)
68. A.Y. Vorobyev, C. Guo, Femtosecond laser nanostructuring of metals. *Opt. Express* **14**, 2164 (2006)
69. J. Vincenc Oboňa, V. Ocelík, J.C. Rao, J.Z.P. Skolski, G.R.B.E. Römer, A.J. Huis In't Veld, J.T.M.D. Hosson, Modification of Cu surface with picosecond laser pulses. *Appl. Surf. Sci.* **303**, 118 (2014)
70. A.Y. Vorobyev, C. Guo, Enhanced absorptance of gold following multipulse femtosecond laser ablation. *Phys. Rev. B* **72**, 195422 (2005)
71. Y. Dai, M. He, H. Bian, B. Lu, X. Yan, G. Ma, Femtosecond laser nanostructuring of silver film. *Appl. Phys. A* **106**, 567 (2012)
72. Q.-Z. Zhao, S. Malzer, L.-J. Wang, Self-organized tungsten nanospikes grown on subwavelength ripples induced by femtosecond laser pulses. *Opt. Express* **15**, 15741 (2007)
73. Y. Ashkenazy, R.S. Averback, Kinetic stages in the crystallization of deeply undercooled body-centered-cubic and face-centered-cubic metals. *Acta Mater.* **58**, 524 (2010)